Chemical Engineering Journal 210 (2012) 120–135

Contents lists available at SciVerse ScienceDirect

Chemical Engineering Journal

journal homepage: www.elsevier.com/locate/cej

Continuous species transport and population balance models for first drying stage of nanosuspension droplets

M. Mezhericher [a,b], M. Naumann [c], M. Peglow [c], A. Levy [b,*], E. Tsotsas [c], I. Borde [b]

[a] Department of Mechanical Engineering, Shamoon College of Engineering, Bialik/Basel Sts., Beer-Sheva 84100, Israel
[b] Pearlstone Centre for Aeronautical Engineering Studies, Department of Mechanical Engineering, Ben-Gurion University of the Negev, P.O. Box 653, Beer-Sheva 84105, Israel
[c] Thermal Process Engineering, Otto von Guericke University, Universitätsplatz 2, 39106 Magdeburg, Germany

HIGHLIGHTS

- Two modelling approaches for nanosuspension droplet drying are compared.
- Continuous species transport approach uses diffusion equation for nanoparticles.
- Alternatively, population balance model deals with nanoparticles as a population.
- Both models were successively validated using published and new experimental data.
- Without aggregation, differences in the two model parametric predictions are minor.

ARTICLE INFO

Article history:
Received 16 May 2012
Received in revised form 12 August 2012
Accepted 14 August 2012
Available online 23 August 2012

Keywords:
Droplet drying
Diffusion
Heat transfer
Mass transfer
Nanoparticle
Population balance

ABSTRACT

The present contribution reports on comparison and verification of two different modelling approaches to intra-droplet mass transfer for nanosuspension droplet drying in the constant-rate period. The first approach is continuous species transport (CST) modelling coupling external gas-droplet heat and mass transfer to a species transport equation of intra-droplet diffusion of nanoparticles. The second approach is a population balance (PB) model with similar description of external heat and mass transfer from gas to droplet. In contrast to the CST model, the PB approach deals with dispersed particles as a population and accounts for the change of nanoparticle distribution by possible aggregation. Both CST and PB models have been successively validated using published and new experimental drying data on single silica nanosuspension droplet. A parametric study revealed insignificant differences in the predicted temporal evolutions of solid volume fraction profiles and values of locking point between the two models when aggregation was "turned off" in the PB model. These small differences can be explained by different mathematical formulations and numerical implementations of the two modelling approaches. A larger contrast between the CST and PB models is the predicted duration of the first drying stage, which has been found to be longer in the case of CST approach. Such divergence is explained by the absence of a shell shrinkage period in the current PB formulation. When applied with aggregation, the PB model can predict the experimentally observed decrease in the diffusion coefficient after the gelation point.

1. Introduction

Particle engineering processes involving droplets containing dispersed nano-sized particles is a field of growing interest in nowadays industry. Spray drying, spray pyrolysis, combined spray-fluidized bed granulation, fluidized bed drying, aerosol thermolysis and freeze drying may utilise nanoparticle suspensions to produce micro-sized particles and coated particulates [1–5]. However, behind these technologies are complex physical phenomena of multiphase heat and mass transport inside and outside of a single droplet. The external transport phenomena have been extensively studied until now [6–12] and include convective and radiative heat flow towards the droplet, and convective species transfer from the droplet outer surface. In contrast, the governing internal transport phenomena are much more sophisticated because of simultaneous heat transport by thermal conduction, diffusive and advective motion of liquid and nanoparticles, aggregation of nanoparticles into bigger conglomerates, agglomeration of nanoparticles leading to

* Corresponding author.
E-mail addresses: maksime@sce.ac.il, mezher@post.bgu.ac.il (M. Mezhericher), martina.naumann@student.uni-magdeburg.de (M. Naumann), mirko.peglow@vst.uni-magdeburg.de (M. Peglow), avi@bgu.ac.il (A. Levy), evangelos.tsotsas@vst.uni-magdeburg.de (E. Tsotsas), borde@bgu.ac.il (I. Borde).

1385-8947/$ - see front matter © 2012 Elsevier B.V. All rights reserved.
http://dx.doi.org/10.1016/j.cej.2012.08.038

Nomenclature

a	internal shell radius (m)
A	correction factor for the combined diffusion coefficient (–)
A_a	cross-sectional area of particle agglomerate (m^2)
b	external shell radius m
B	Spalding number (–)
B_a	circumference of agglomerate (m)
B_{agg}	birth term of aggregation ($m^{-3}\ s^{-1}$)
C	mass concentration ($kg\ m^{-3}$)
c_p	specific heat under constant pressure ($J\ kg^{-1}\ K^{-1}$)
d	diameter (m)
D_{agg}	death term of aggregation ($m^{-3}\ s^{-1}$)
D_{ls}	diffusion coefficient of liquid in droplet ($m^2\ s^{-1}$)
D_p	diffusion coefficient of nanoparticles in droplet ($m^2\ s^{-1}$)
D_v	diffusion coefficient of liquid vapour in ambient ($m^2\ s^{-1}$)
h	heat transfer coefficient ($W\ m^{-2}\ K^{-1}$)
h_D	mass transfer coefficient ($m\ s^{-1}$)
h_{fg}	latent heat of evaporation ($J\ kg^{-1}$)
j_v	flux of dispersed particles with respect to the internal coordinate (s^{-1})
k	thermal conductivity ($W\ m^{-1}\ K^{-1}$)
$k_B = 1.3806488 \times 10^{-23}\ J\ K^{-1}$	Boltzmann constant
L	outer radius of submerged agglomerated shell (m)
m	mass (kg)
M	molecular weight ($kg\ mol^{-1}$)
$\dot{m}_v$	rate of evaporation ($kg\ s^{-1}$)
n	number density (m^{-3})
N_c	total number concentration = number of particles/droplet volume (m^{-3})
N_r	number of discretized elements in spatial direction (–)
N_v	number of discretized elements in internal direction (–)
Nu	Nusselt number (–)
p	pressure (Pa)
$Pr = \frac{\nu_g}{\alpha_g}$	Prandtl number (–)
r	spatial coordinate (m)
R	radius (m)
$\Re = 8.314\ J\ mol^{-1}\ K^{-1}$	universal gas constant
$Re = \frac{v_g d_d}{\nu_g}$	Reynolds number (–)
S	volumetric rate of a homogeneous chemical reaction ($kg\ m^{-3}\ s^{-1}$)
$Sc = \frac{\nu_g}{D_v}$	Schmidt number (–)
Sh	Sherwood number (–)
S_v	specific surface area (m^{-1})
t	time (s)
T	temperature (K)
u	internal coordinate (particle volume, PB model) (m^3)
v	velocity; internal coordinate (particle volume, PB model) ($m\ s^{-1}$; m^3)
V	volume m^3
$\bar{v}$	volume-averaged velocity ($m\ s^{-1}$)
$\dot{V}$	volumetric flow rate ($m^3\ s^{-1}$)
w	local shrinkage rate of control volume ($m\ s^{-1}$)
X	moisture content of droplet/particle (dry basis) ($kg\ kg^{-1}$)
Y	moisture content of drying medium ($kg\ kg^{-1}$)

Greek letters

α	angle; thermal diffusivity (–; $m^2\ s^{-1}$)
β	empirical coefficient; coefficient of thermal expansion (–; K^{-1})
β^*	aggregation kernel (s^{-1})
β_0	aggregation constant (s^{-1})
γ	surface tension; normalised droplet radius ($N\ m^{-1}$; –)
ε	crust porosity (–)
θ	contact angle (–)
μ	dynamic viscosity ($kg\ m^{-1}\ s^{-1}$)
ν	kinematic viscosity ($m\ s^{-2}$)
ξ	correction factor (–)
ρ	density; curvature ($kg\ m^{-3}$; m)
σ	stress (Pa)
$[\sigma_c]$	compressive strength (Pa)
φ	volume fraction ($m^3\ m^{-3}$)
χ	normalised number density (–)
ψ	coordinate angle (–)
ω	mass fraction ($kg\ kg^{-1}$)

Subscripts

a	air
agg	aggregation
c	capillary
cr	crust; critical
d	droplet
$diff$	diffusion
ext	external
f	final
$flow$	flow
g	drying medium
gl	glass tube
i	crust–wet core interface
int	internal
l	liquid fraction
$lock$	point of nanoparticles "locking"
m	air–vapour mixture
p	particle
pp	primary particle (nanoparticle)
r	radial direction
s	solid fraction; surface
sat	saturated
sh	shell
v	vapour
w	water
wc	wet core
ψ	tangential direction
0	initial
∞	bulk of drying medium

formation of a wet assembly of primary particles (shell) turning eventually into a dehumidified particle arrangement (dry crust), liquid diffusion and flow through the crust pores. Moreover, the above phenomena are complicated by the droplet shrinkage and structural transformation (droplet turns into a wet particle comprising crust and wet core regions). Bubble growth within the wet particle, distortion of the particle shape and the particle cracking/breakage are supplementary factors affecting transport phenomena and obtained product quality.

The review of published literature on theoretical drying modelling of single droplets containing suspended submicron particles demonstrates that there are two principal modelling approaches for treatment of intra-droplet transport phenomena and predicting time-changing profiles of suspended particles: continuous species transport (CST) and population balance (PB) techniques. The CST models are based on continuous description of coupled external heat and mass transfer from gas to droplet and species transport equation for intra-droplet mass transfer of suspended particles

[13–19]. In turn, the PB model is underpinned by continuous description of coupled external heat and mass transfer from gas to droplet and population balance approach for the intra-droplet mass transfer phenomenon [20–24]. It should, however, be noted that the PB approach has only been applied to growth of suspended particles in droplet until the very recent treatment of aggregation by Bück et al. [25].

One of the advantages of CST approach is its suitability for modelling of both suspension and solution droplets drying [15]. However, it neglects growth and aggregation effects between suspended particles that increase with reduction of the particles to nano-scale sizes [26,27] and may substantially affect the intra-droplet particles motion and, consequently, change the moment of shell formation and obtained particle morphology. In contrast, PB modelling takes into account the phenomena of growth and aggregation which, however, may be unimportant for treating the drying of solution droplets. The common benefit of both CST and PB formulations is their suitability to be coupled to models of external transport phenomena in multiphase flow with droplets and particles to describe thermally-assisted processes of particles engineering at multiple scales (a detailed discussion on importance of multi-scale modelling for drying processes is given by Perré [28]).

To the best of our knowledge, until now a detailed investigations devoted to comparison between CST and PB models have not been published. The predictions of drying kinetics by both approaches are expected to coincide for the same case studies of nanosuspension droplet drying with "turned off" aggregation and growth terms in the PB formulation. On the other hand, the CST and PB approaches are foreseen to calculate different duration of the first drying stage if the aggregation and growth of suspended particles are considered.

2. Study objectives

The central idea of the present work is comparison and verification of two different approaches of intra-droplet mass transfer description for nanosuspension droplet drying in constant-rate period of moisture fall: continuous species transport and population balance models. The CST model is based on continuous formulation of coupled external heat and mass transfer from gas to droplet and species transport equation for intra-droplet mass transfer of nanoparticles. In turn, the PB model is underpinned by continuous description of coupled external heat and mass transfer from gas to droplet and population balance approach for the intra-droplet mass transfer phenomenon.

3. Theoretical modelling

3.1. Governing equations of external heat and mass transfer

In this work a spherical droplet containing liquid with suspended nano-scaled particles is evaporated by surrounding hot gas medium. Assuming a uniform droplet temperature, the droplet energy balance during the first drying stage is given by:

$$h_{fg}\dot{m}_v + c_{p,d} m_d \frac{dT_d}{dt} = h(T_g - T_d)4\pi R_d^2, \tag{1}$$

The droplet shrinkage due to evaporation is considered to be isotropic and thus the droplet preserves its spherical shape. The rates of droplet evaporation flow and shrinkage are determined as follows [29]:

$$\dot{m}_v = h_D(\rho_{v,s} - \rho_{v,\infty})4\pi R_d^2, \tag{2}$$

$$\frac{dR_d}{dt} = -\frac{1}{\rho_{d,w} 4\pi R_d^2}\dot{m}_v. \tag{3}$$

Denoting gas moisture content on dry basis (also known as specific humidity, see Cengel and Boles [30]) by

$$Y_g = \frac{m_v}{m_a} = \frac{\rho_v}{\rho_a}, \tag{4}$$

and neglecting the difference between the dry air densities at the droplet surface and in the bulk (i.e., $\rho_{a,s} \simeq \rho_{a,\infty}$), we get:

$$\dot{m}_v = h_D \rho_{a,\infty}(Y_{g,s} - Y_{g,\infty})4\pi R_d^2, \tag{5}$$

$$\frac{dR_d}{dt} = -h_D \frac{\rho_{a,\infty}}{\rho_{d,w}}(Y_{g,s} - Y_{g,\infty}), \tag{6}$$

Eq. (5) demonstrates the driving force for the mass transfer, which is given by the difference between the gas moisture content at the droplet surface (equal to the corresponding adiabatic saturation moisture content), $Y_{g,s}$, and the moisture content in the bulk of the surrounding gas phase, $Y_{g,\infty}$.

The coefficients of heat and mass transfer are calculated from the Nusselt and Sherwood dimensionless groups. These values are determined using the modified Ranz–Marshall correlations appropriate for evaporating spherical droplets [31]:

$$Nu_d = \frac{2hR_d}{k_g} = (2 + 0.6Re_d^{1/2}\mathrm{Pr}^{1/3})(1+B)^{-0.7}, \tag{7}$$

$$Sh_d = \frac{2h_D R_d}{D_v} = (2 + 0.6Re_d^{1/2}Sc^{1/3})(1+B)^{-0.7}, \tag{8}$$

where $B = c_{p,v}(T_g - T_d)/h_{fg}$ is the Spalding number accounting for the effect of Stefan flow from the droplet surface. It is worth noting that the influence of thermal radiation on the overall rate of heat transfer is disregarded since it was found to be important only for large droplets >1 mm and high drying temperatures >400 °C [12].

For drying of aqueous droplets in atmospheric air, the coefficient of vapour diffusion in the surroundings may be evaluated by [32]:

$$D_v = 3.564 \times 10^{-10}(T_d + T_g)^{1.75}, \tag{9}$$

where the temperatures are in Kelvin.

3.2. Intra-droplet mass transfer: continuous species transport (CST) approach

The CST approach for intra-droplet mass transfer in aqueous droplets with suspended nanoparticles subjected to evaporation was at first presented by Mezhericher et al. [19]. In the present contribution this approach is adopted and compared with alternative population balance method. For the reader convenience, the theoretical concept and the model main equations are given below.

According to Cussler [33], a general mass balance of continuous liquid fraction within two-component droplet can be written as follows:

$$\frac{\partial C_l}{\partial t} + \nabla \cdot C_l \bar{v} = D_{ls}\nabla^2 C_l + S_l. \tag{10}$$

Here C_l is mass concentration of the liquid fraction, D_{ls} is its diffusivity, $\bar{v}$ is liquid velocity (volume-averaged) and S_l is a liquid source term. The adopted assumptions for the current research are: to neglect the liquid circulation within the droplet, to disregard the production of liquid component and to presume that quantity of acts of nanoparticle spontaneous agglomerations is negligible. Furthermore, if we consider a spherical symmetry of the phenomena,

Eq. (10) can be rendered to the well-known Fick second law of diffusion:

$$\frac{\partial C_l(r,t)}{\partial t} = \frac{1}{r^2}\frac{\partial}{\partial r}\left[r^2 D_{ls}\frac{\partial C_l(r,t)}{\partial r}\right], \tag{11}$$

where $0 \leqslant r \leqslant R_d(t)$. As an initial condition for this differential equation, a uniform liquid concentration at the beginning of the droplet evaporation may be assumed. The boundary conditions for Eq. (11) are derived using the problem symmetry and the conservation of the droplet solid mass:

$$\begin{cases} \frac{\partial C_l(r,t)}{\partial r} = 0, & r = 0; \\ \frac{\partial}{\partial t}\left[\int_0^{R_d(t)} C_s(r,t) 4\pi r^2 dr\right] = 0, & r = R_d(t). \end{cases} \tag{12}$$

Here C_s is the mass concentration of solid fraction. Considering the constant densities of solid and liquid fractions and using the relation $C_s = \rho_s(1 - C_l/\rho_l)$, Eq. (12) yields [34]:

$$\begin{cases} \frac{\partial C_l(r,t)}{\partial r} = 0, & r = 0; \\ -D_{ls}\frac{\partial C_l(r,t)}{\partial r} + [\rho_l - C_l(r,t)]\frac{dR_d(t)}{dt} = 0, & r = R_d(t). \end{cases} \tag{13}$$

According to the theory proposed by Mezhericher et al. [19], during the droplet evaporation the concentration of the solid component near the droplet surface increases continuously. At some moment this concentration reaches a saturation (so called "locking point"), a shell of agglomerated primary particles is formed and a *transition period* begins. It is noted that at the moment of this initial shell formation the shell is submerged into the liquid and the liquid is evaporated from the droplet surface until liquid menisci between the agglomerated primary particles appear (Fig. 1). These concave liquid menisci produce capillary forces acting along tangential and radial shell directions. In turn, the tangential components of the capillary forces pull shell particles one to another and, correspondingly, produce *compressive tangential stresses* in the shell. Additionally, radial components of capillary forces are pointed at the droplet centre and lead to *compressive radial stresses* in the shell. Therefore, the shell undergoes compression in both tangential and radial directions which may result in the shell buckling inward and shrinkage (the discussion on criterion of the shell shrinkage is given below in this section). If the shell shrinks, its particles will sink into the liquid and then a liquid layer will cover the contracted shell, see Fig. 2. Subsequently, the liquid will be freely evaporated from the droplet surface by the ambient until the liquid level is decreased again to create menisci between the shell particles. Once more, these menisci may cause the shell shrinking and submerging into the liquid, and then again the liquid will evaporate from the droplet surface, and after that menisci will appear on the droplet surface, and then shell may contract and so forth. In that way, the droplet evaporation in the transition period may comprise of many series of alternating steps of liquid evaporation from the droplet surface and shell shrinkage. However, the characteristic time scale of the liquid surface evaporation can be considered to be substantially greater than that of the shell shrinkage [19], and correspondingly the shell shrinkage and submergence can be assumed to occur instantly after the menisci appearance at the droplet surface. Owing to the feature of rapid shell submergence, the evaporation from the droplet surface occurs almost throughout the whole transition period, and thus the droplet temperature should remain at the same level of equilibrium evaporation temperature (adiabatic saturation/wet bulb temperature) as it was before the shell formation. For this reason, the rate of droplet evaporation per unit area is preserved equal to the same steady value as before the transition period. Consequently, Eqs. (1)–(11) are applicable for the transition period. However, it is noted that Eqs. (10) and (11) are valid for the droplet regions not including the shell $0 \leqslant r \leqslant R_{sh}(t)$. Moreover, instead of Eq. (13), the following boundary conditions are applied for the liquid diffusion equation (11) [19]:

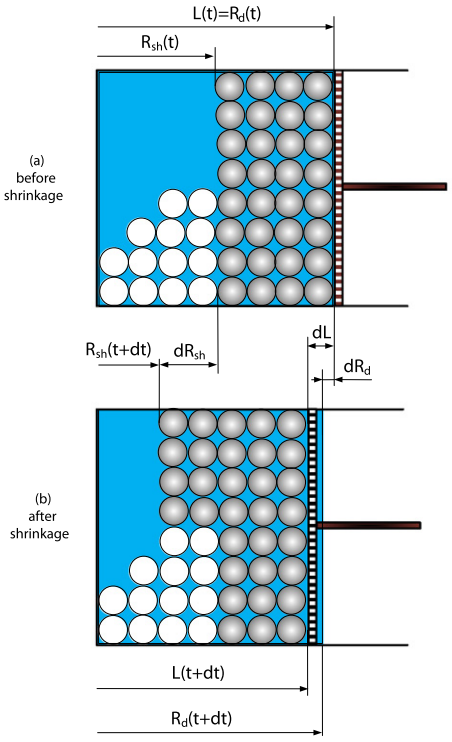

Fig. 2. Mechanical analogy illustrating the shell shrinkage concept [19].

$$\begin{cases} \frac{\partial C_l(r,t)}{\partial r} = 0, & r = 0; \\ \frac{\partial C_l(r,t)}{\partial r} = 0, & r = R_{sh}(t); \end{cases} \tag{14}$$

$$\begin{cases} C_l(r,t) = C_{l,cr} = \rho_l \varepsilon, & R_{sh}(t) < r \leqslant L(t); \\ C_l(r,t) = \rho_l, & L(t) < r \leqslant R_d(t). \end{cases} \tag{15}$$

Here R_{sh} and $L(t)$ are internal and outer radii of the submerged shell.

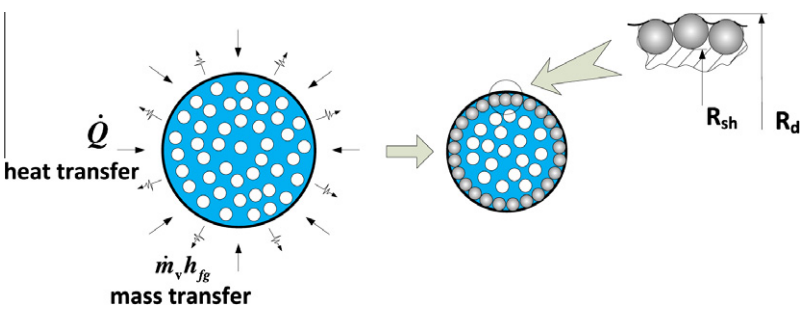

Fig. 1. Shell formation and appearance of liquid menisci at droplet surface [19].

When the shell of agglomerated primary particles buckles and shrinks under the compressive capillary stresses, the shell becomes thicker and stronger. And if the shell strength will overcome the capillary compression, the shell contraction will cease. Then, as the result of the ongoing liquid evaporation, the evaporation interface will move from the droplet outer surface toward the droplet centre, and, subsequently, the non-shrinking shell will dehydrate and turn into a dry crust. In this moment the second drying stage begins – the droplet becomes a wet particle comprising crust and wet core; however, this stage is out of scope of the present contribution.

To determine mechanical stresses appearing in shell during the transition period between the first and second drying stages, the shell of agglomerated nanoparticles is considered as a pseudo-continuous solid spherical body. Consequently, the intra-shell mechanical stresses caused by internal and external pressures are calculated as follows [35]:

$$\sigma_r(r,t) = p_{ext}(t)\frac{b^3(r^3-a^3)}{r^3(a^3-b^3)} + p_{int}(t)\frac{a^3(b^3-r^3)}{r^3(a^3-b^3)}, \tag{16}$$

$$\sigma_\psi(r,t) = p_{ext}(t)\frac{b^3(2r^3+a^3)}{2r^3(a^3-b^3)} - p_{int}(t)\frac{a^3(2r^3+b^3)}{2r^3(a^3-b^3)}. \tag{17}$$

Here a and b are internal and external radii of the shell, respectively, and $a \leqslant r \leqslant b$.

The external pressure on the shell, p_{ext}, is produced by capillary forces and liquid surface tension:

$$p_{ext} = p_c + p_s. \tag{18}$$

For particle agglomerates, the capillary pressure is equal to [36]:

$$p_c = \frac{\gamma_{lv} S_v (1-\varepsilon)}{\varepsilon}\cos\theta, \tag{19}$$

In the studied case, the primary particles are uniform spheres and thus the specific surface area $S_v = 6/d_{pp}$, which yields [36,17]:

$$p_c = \frac{6\gamma_{lv}}{d_{pp}}\left(\frac{1-\varepsilon}{\varepsilon}\right)\cos\theta. \tag{20}$$

The contribution of the surface tension to the external pressure is given by [36]:

$$p_s = \frac{B_a \gamma_{lv}}{A_a}\cos\theta, \tag{21}$$

where $B_a = 2\pi R_d(t)$ and $A_a = \pi R_d^2(t)$ are circumference and cross-sectional area of the agglomerate, respectively. Hence, combining Eqs. (20) and (21), we get:

$$p_{ext}(t) = 2\gamma_{lv}\cos\theta\left[\frac{3}{d_{pp}}\left(\frac{1-\varepsilon}{\varepsilon}\right) + \frac{1}{R_d(t)}\right]. \tag{22}$$

The internal pressure acting on the shell, p_{int}, is caused by the droplet internal pressure, which is related to the curvature of the liquid–air interface and determined according to the well-known Laplace–Young equation:

$$p_{int}(t) = \frac{2\gamma_{lv}}{R_d(t)}. \tag{23}$$

Now the distribution of mechanical stresses within this spherical shell can be calculated using Eqs. (16), (17), (22) and (23). However, a supplementary effect should be taken into consideration: for the outer layer of the shell particles the capillary effects are leading to additional inter-particle attractive force, and, correspondingly, auxiliary stress, in tangential direction. To derive a mathematical expression for this stress let us consider a liquid bridge between two spherical particles, Fig. 3. The capillary force is given by [37]:

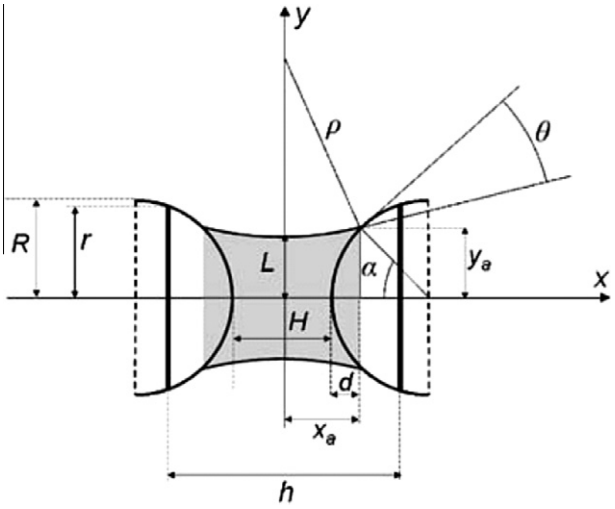

Fig. 3. Liquid bridge between two primary particles [37].

$$F_c = -\pi\gamma_{lv}R_{pp}\sin\alpha\left[2\sin(\alpha+\theta) + R_{pp}\left(\frac{1}{L}-\frac{1}{\rho}\right)\sin\alpha\right], \tag{24}$$

where

$$\rho = \frac{x_a}{\cos(\alpha+\theta)},\ L = y_a + \rho[1-\sin(\alpha+\theta)]\ \ and\ \ R_{pp} = \frac{d_{pp}}{2}. \tag{25}$$

In Eq. (24), the first term expresses the surface tension force and the second term is the force emerging due to the pressure difference across the curved gas–liquid interface.

Therefore, the additional tangential compressive stress in the shell outer layer can be evaluated as follows:

$$\sigma_{\psi,c}(r=R_d,t) = \frac{F_c}{\pi R_{pp}^2\sin^2\alpha} = -\frac{2\gamma_{lv}\sin(\alpha+\theta)}{R_{pp}\sin\alpha} - \gamma_{lv}\left(\frac{1}{L}-\frac{1}{\rho}\right). \tag{26}$$

As a result, the total tangential stress at the droplet surface is found by summarizing Eqs. (17) and (26):

$$\sigma_\psi(r=R_d,t) = \frac{p_{ext}b^3(2R_d^3+a^3)}{2R_d^3(a^3-b^3)} - \frac{p_{int}a^3(2R_d^3+b^3)}{2R_d^3(a^3-b^3)} - \frac{2\gamma_{lv}\sin(\alpha+\theta)}{R_{pp}\sin\alpha} - \gamma_{lv}\left(\frac{1}{L}-\frac{1}{\rho}\right). \tag{27}$$

And finally, in the transition period two principal situations can take place [19]:

(a) Dynamic non-equilibrium, when maximum shell stress is greater than the shell compressive strength: $\max\{\sigma_r(r,t), \sigma_\psi(r,t)\} > [\sigma_c]$. The shell collapses and submerges into the liquid due to menisci capillary pressure whereas the liquid evaporates from the droplet surface. Owing to the shrinkage, the shell becomes thicker and stronger. The rate of shell contraction is given by [19]:

$$\frac{dR_{sh}}{dt} = \frac{1-\varepsilon}{\varphi_l|_{R_{sh}} - \varepsilon}\frac{R_d^2}{R_{sh}^2}\frac{dR_d}{dt}. \tag{28}$$

Here $\varphi_l|_{R_{sh}}$ is liquid volume fraction at the new shell internal radius.

(b) Static equilibrium, when maximum shell stress is either equal or smaller than the shell compressive strength: $\max\{\sigma_r(r,t), \sigma_\psi(r,t)\} \leqslant [\sigma_c]$. In this case, the shell undergoes

only compressive elastic deformation. The appearance of such static equilibrium indicates the end of transition period and beginning of the second drying stage, in which the liquid evaporation occurs not from the surface but in the wet particle interior.

3.3. Intra-droplet mass transfer: population balance (PB) approach

The intra-droplet mass transfer during the droplet drying process depends on several parameters among them the distribution of dispersed particles and their characteristic volumes. In the present population balance model it is assumed that the droplet structure remains radially symmetrical during drying and thus gradient of particle concentration exists only in radial direction, r, of the droplet. Furthermore, it is supposed that diffusion is the dominating transport phenomenon and correspondingly convective mass transfer of suspended nanoparticles is neglected. Additionally, the volume of suspended particle, v, is chosen to be an internal coordinate.

Using the above assumptions, the temporal evolution of the number density of dispersed nanoparticles in the droplet, $n(v,r,t)$, can be described by the standard population balance equation [38]:

$$\frac{\partial n}{\partial t} = \frac{1}{r^2}\frac{\partial}{\partial r}\left(D_p r^2 \frac{\partial n}{\partial r}\right) - \frac{\partial j_v}{\partial v} + B_{agg}(n,v,r,t) - D_{agg}n,\ v,r,t), \tag{29}$$

where $0 \leqslant r \leqslant R_d$ and $0 \leqslant v < \infty$.

Regarding the kind and size of the suspended nanoparticles, in the present study it is assumed that the nanoparticles cannot grow or break during the drying process, i.e. $j_v = 0$. Furthermore, the birth term and death term of aggregation are expressed as follows:

$$B_{agg}(n,v,r,t) = \frac{1}{2}\int_0^v \beta^*(u, v-u)n(u,r,t)n(v-u,r,t)du, \tag{30}$$

$$D_{agg}(n,v,r,t) = \int_0^\infty \beta^*(u,v)n(v,r,t)n(u,r,t)du. \tag{31}$$

The value of agglomeration kernel, β^*, depends on applied law of underlying process (e.g., constant kernel, sum kernel or product kernel).

The boundary conditions for the PB equation (29) are given by:

$$\begin{cases} \frac{\partial n}{\partial r} = 0, & r = 0; \\ \frac{d}{dt}\left[\int_0^{R_d}\int_0^\infty n(v,r,t)4\pi r^2 dr dv\right] = 0, & r = R_d. \end{cases} \tag{32}$$

However, the formulation of the population balance as given by Eq. (29) is valid only for a constant control volume. In the current case the volume is time-dependent $R_d = f(t)$ because of the drying process. For this reason a more general equation of population balance should be used instead of Eq. (29) (see [39] for details on derivation of partial differential equations from conservation laws):

$$\frac{d}{dt}\int_0^{R_d(t)} n dr = \int_0^{R_d(t)} \left[\frac{1}{r^2}\frac{\partial}{\partial r}\left(D_p r^2 \frac{\partial n}{\partial r}\right) + B_{agg}(n,v,r,t) - D_{agg}(n,v,r,t)\right] dr. \tag{33}$$

The application of Leibnitz's rule for differentiation under the integral sign [40] yields:

$$\frac{\partial n}{\partial t} + \frac{1}{r^2}\frac{\partial}{\partial r}(r^2 w n) = \frac{1}{r^2}\frac{\partial}{\partial r}\left(r^2 D_p \frac{\partial n}{\partial r}\right) + B_{agg}(n,v,r,t) - D_{agg}(n,v,r,t). \tag{34}$$

In contrast to Eq. (29), the above Eq. (34) is valid for the time-dependent domain $0 \leqslant r \leqslant R_d(t)$ and $0 \leqslant v < \infty$. The second left-hand side term in Eq. (34) accounts for the change in the number density due to the local droplet volume change. In this term, the local shrinkage rate of the control volume, w, is given by:

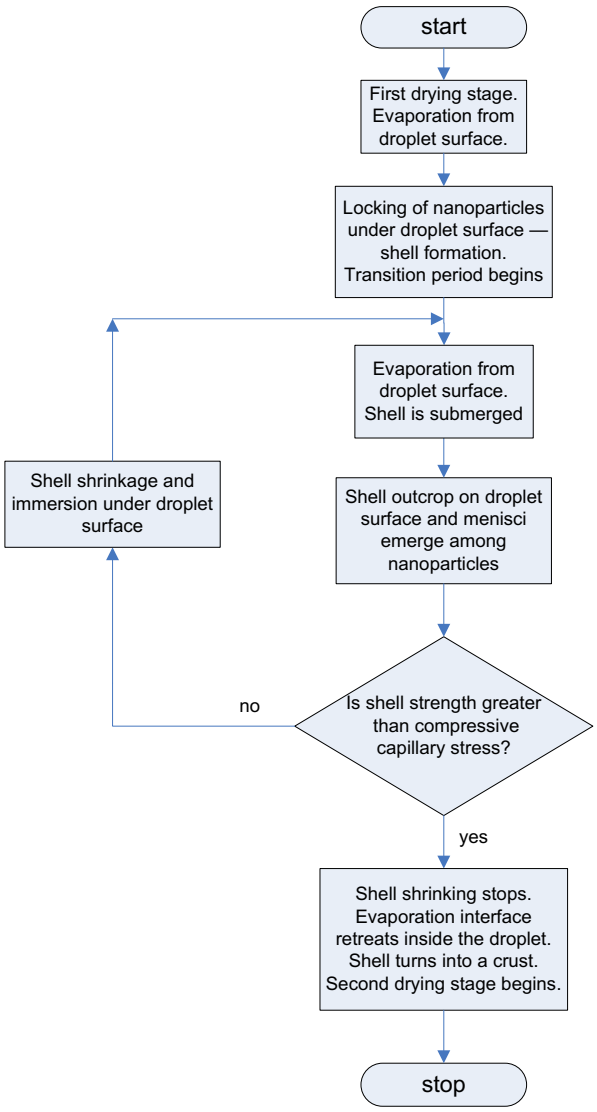

Fig. 4. Flowchart of solution algorithm for CST model of droplet drying [19].

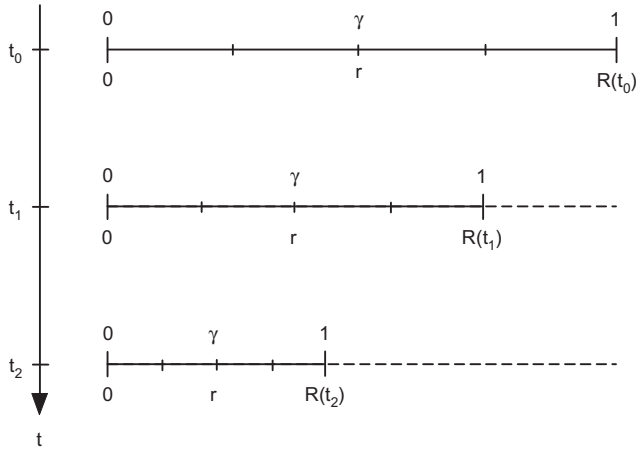

Fig. 5. Illustration of the moving grid implementation: at each time step of the simulation the remaining droplet radius is divided into N_r control volumes of equal width. The velocity of the moving grid is the same as the shrinkage rate of the droplet [25].

$$w = \begin{cases} 0, & r \neq R_d(t); \\ \frac{dR_d}{dt}, & r = R_d(t). \end{cases} \quad (35)$$

Finally, for Eq. (34) the following boundary conditions are derived:

$$\begin{cases} \frac{\partial n}{\partial r} = 0, & r = 0; \\ \frac{d}{dt}\left[\int_0^{R_d(t)} \int_0^{\infty} n(v,r,t) 4\pi r^2 dr dv\right] = 0, & r = R_d(t). \end{cases} \quad (36)$$

4. Numerical solution

4.1. Continuous species transport approach

The numerical solution used here was chosen based on the previous studies [19,29]. In particular, the ordinary differential equation (1) of droplet energy balance coupled to Eqs. (2) and (3) was numerically solved using the Runge–Kutta method of the fourth order accuracy [41]. The partial differential equation (PDE) of liquid fraction diffusion (11) was discretized using a Crank–Nicolson finite difference numerical method (second order accuracy in space and first order in time) with a fixed time-step, and the solution procedure was based on the Moyano and Scarpettini [42] algorithm specially developed for parabolic PDEs with moving boundaries. The unconditional convergence and stability of the numerical scheme allowed choosing the value of fixed time-step in the following simple way: the approximate experimental duration of the first drying stage was divided into 1000 equal time steps. Such temporal resolution was found to be enough to provide accurate predictions of droplet evaporation histories. Fig. 4 demonstrates the devised solution algorithm for CST model equations. It is worth noting that compared to the previous study [19], the computer implementation of the numerical solution has been revised and

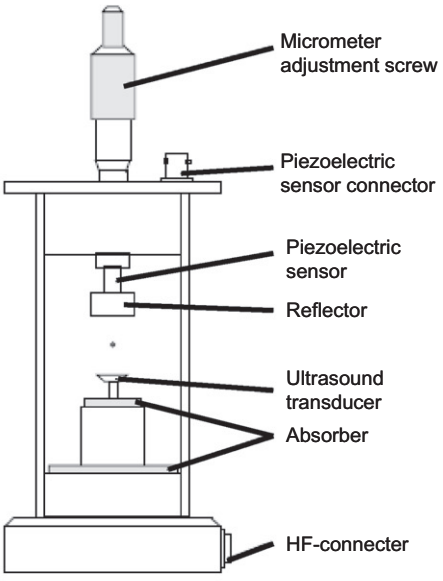

(a)

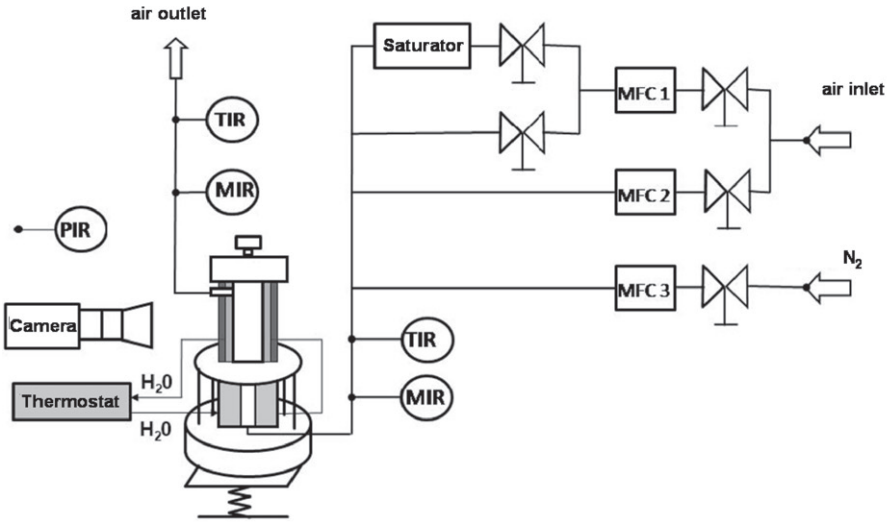

(b)

Fig. 6. Schematic sketchs of (a) acoustic levitator and (b) experimental setup.

refined by demanding to preserve the overall solid mass within the evaporating droplet more rigorously.

4.2. Population balance approach

In order to solve numerically the PB model Eqs. (34)–(36), discretization is performed with respect to both the internal property (volume of particles) and the external (droplet radius) coordinate. Consequently, N_r mesh nodes are used in the droplet radial direction and N_v nodes are in the direction of the property coordinate. Furthermore, Eq. (34) is treated by finite volume method for parabolic PDEs [39] except the integral aggregation terms B_{agg} and D_{agg} handled by the Cell Average method [43].

To facilitate the solution of the developed PB formulation which is classified as a moving boundary problem because of time-dependent solution domain $0 \leqslant r \leqslant R_d(t)$ (see [44]), and to avoid the appearance of numerical difficulties due to the different orders of magnitude in the discretized property distribution and the droplet radius, the following scalings are introduced:

$$\gamma = \frac{r}{R_{d,0}} \quad \text{and} \quad \chi = \frac{n}{n_0}, \tag{37}$$

where $R_{d,0}$ the initial droplet radius and n_0 the initial total number density. These new coordinates are dimensionless, $0 \leqslant \gamma \leqslant 1$, $0 \leqslant \chi \leqslant 1$, and the numerical solution of the PB model is implemented on a moving grid (see Fig. 5).

The PB model equations have been integrated in two steps. At first, the PDE (34) is converted to the set of ODEs (ordinary differential equation) using a second-order accurate spatial discretization based on a fixed set of user-specified nodes [45]. Then, the time integration is done by means of the MATLAB "ode15s" adaptive solver that realises a variable-order numerical differentiation scheme [46]. Consequently, the PB formulation has been discretized using the second order accuracy in space and first to fifth order adaptive precision in time. Finally, the computer program implementing the numerical solution has been developed in such way that all the physical phenomena included in the PB model (drying, diffusion and aggregation) can be individually switched on or off.

5. Experimental

For further validation of both the CST and the PB models of droplet drying kinetics, a series of laboratory experiments on single droplet drying were carried out using an acoustic levitator setup (Ultrasonic Levitator 13L10, Dantec/Invent, Erlangen, DE) – an equipment that already proved itself as a useful instrument for determination of single droplet drying curves suitable for practical design applications [47]. In this apparatus (see Figs. 6 and 7) the droplet is levitated by means of a supporting pressure generated by an acoustic wave of ultrasonic frequency range. The levitator was integrated with a contact angle measurement device (OCA 15Pro, Dataphysics, Filderstadt, DE) on a table that can be adjusted in all three spatial directions. Such integration enabled to use the levitator with an electronic droplet dosage system that allows precise dispensing of a selected volume of solution or suspension. Furthermore, there is a high speed camera (Navitar®) connected to a computer to capture the droplet images during the experiment. One may observe that the experimental installation is rather compact compared to widely-spread bulky methods for drying kinetics measurement, e.g. drying tunnel [48].

The main parts of the levitator are an ultrasonic transducer with a working frequency of 58 kHz and a reflector. The transducer is located at the top and the reflector is situated at the bottom of the process chamber enclosed by a glass cylinder to prevent gas leakages. To provide the desired air temperature inside the chamber, the whole system is surrounded by a heat exchanger coil and insulated by a polyurethane cylinder. The moisture of the drying gas flowing through the levitator is measured at the inlet (via a dew point hygrometer) and at the outlet (via an infrared spectroscope) of the levitation device. Furthermore, the temperature of the drying gas is sampled at the outlet of the levitator by means of a thermoelement. To investigate the drying process, the volumetric flow rate, temperature and moisture content of the supplied drying gas can be varied. However, the droplet temperature is not measured in the present experimental studies.

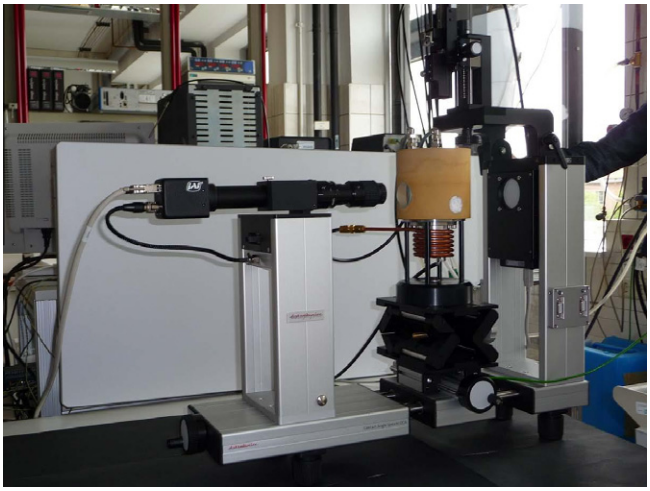

Fig. 7. Photograph of the acoustic levitator installation.

Table 1
Parameters of acoustic levitation experiments.

Drying gas	Atmospheric air
Gas temperature	15, 22 and 35 °C
Gas volumetric flow rate	500 ml/min
Gas moisture content	0.004 kg_w/kg_g
Droplet initial diameter	~1.5 mm
Liquid fraction in droplet	Water
Suspended solids in droplet	200 nm spherical silica particles
Density of solid fraction	2.09 g/cm^3
Initial value of solid mass fraction in droplet	0.05 kg_s/kg_d

It is noted that the droplet in the levitator is slightly elliptical due to the squeezing pressure from the ultrasonic waves. For this reason, a radius of equivalent sphere is determined from the captured droplet image and it is compared to the theoretical predictions. Further, the ultrasonic field induces acoustic streaming around the drying droplet which increases heat and mass transfer to the bulk phase [34]. To consider this phenomenon, the correlation of Möser [49] can be used to accurately calculate the increase in Sherwood number:

$$Sh_d^* = \sqrt{Sh_d^2 + \xi^2}. \tag{38}$$

Here Sh_d^* is the Sherwood number in the acoustic field, Sh_d is the Sherwood number determined by the usual correlation Eq. (8), and ξ is a correction factor taking into account the acoustic streaming. In the present study, it was found that the value $\xi = 1$ (also recommended by Möser [49]) gave a good agreement of calculations with the experimental data.

The main parameters of the acoustic levitation experiments are given in Table 1.

Table 2
Input data used for the validation of CST and PB models.

Droplet	
Initial diameter	2 mm
Initial temperature	19 °C
Initial mass	4.1 mg
Initial solid mass content	30%
Material of suspended particles	SiO_2
Shape of suspended particles	Spherical
Size of suspended particles	16 nm, monosized
Shell porosity at locking point	0.4
Drying air	
Temperature	178 °C
Velocity	1.4 m/s
Relative humidity	0.004

The gas velocity around the levitated droplet was found as follows:

$$v_g = \frac{\dot{V}_g}{(\pi/4)\cdot d_{gl}^2}, \tag{39}$$

where d_{gl} = 15 mm is the diameter of the glass tube surrounding the process chamber and $\dot{V}_g$ is the gas volumetric flow rate. This resulted in the velocity value of v_g = 0.047 m/s, and the corresponding Reynolds number (based on the initial droplet diameter) being in the range of Re_d = 4.3–4.8 for all the performed experiments.

6. Results and discussion

6.1. Validation by published experimental data

To validate the developed continuous species transport and population balance models, the information about drying of 2 mm single silica nanosuspension droplet in atmospheric air published by Nešić [14] and Nešić and Vodnik [15] is used. The input data used for the numerical simulations are given in Table 2.

It is worth noting that the experimental data of Nešić and Vodnik [15] yield a calculated solid density of ρ_s = 925 kg m^{-3}. Though it is an untypical value for the density of silica, it is used nevertheless in the following calculations for best comparison of overall mass and temperature history with the published experimental data.

To predict the beginning of shell growth within the droplet, the "locking" between the suspended nanoparticles and corresponding initial shell formation were assumed to occur at a solid volume fraction of $\varphi_{s,max} = \varphi_{s,sat}$ = 0.6. The latter is known as a maximum theoretical value of solid volume fraction for orthorhombic package of monosized spheres [50]. The corresponding shell porosity is equal to $\varepsilon_{sh} = 1 - \varphi_{s,sat}$ = 0.4. The applied liquid–solid diffusion coefficient is given by [14]:

$$D_{ls} = \begin{cases} 10^{-6}, & \omega_l > 0.6; \\ \exp\left(-\frac{28.1+282\omega_l}{1+15.47\omega_l}\right), & \omega_l \leqslant 0.6. \end{cases} \tag{40}$$

It is noted that the value of diffusion coefficient $D_{ls} = 10^{-6}$ m^2 s^{-1} is assumed to imitate the effect of a vigorous intra-droplet liquid circulation caused by air drag force. This effect was observed by Nešić and Vodnik [15] in their experiments from the beginning of droplet evaporation until the gel structure formation at droplet liquid mass fraction ω_l = 0.6. In addition, it is presumed here that suspension have been initially stabilized, nanoparticles are evenly distributed within a single droplet and do not aggregate between each other during the drying process.

The comparison between the predicted and measured [14] evolutions of silica droplet mass and temperature in the first drying stage are given in Fig. 8. One can establish a good agreement between the calculated curves and experimental points for both CST and PB model predictions of droplet temperature and mass histories. The only difference is that the duration of the first drying stage predicted by the PB model is shorter compared to this of the CST approach. The origin of such dissimilarity is explained in the Section 6.3, where the other droplet parameters are analysed in details.

6.2. Validation by acoustic levitator experiments

The results of comparison between the experimentally determined and predicted evolutions of droplet diameters are shown in Fig. 9. The setup parameters are given in Table 1 and the value of intra-droplet diffusion coefficient is calculated using Eq. (40). Further, the Sherwood number amplified by acoustic field, evaluated by the correlation (38), was found to be in the range of 2.75–2.84.

For the drying air supplied at 15 °C, Fig. 9a shows that the CST model predicts the duration of the first drying stage equal to 2022 s, whereas the value calculated by the PB model is 1902 s, and the corresponding experimental point is at about 1830 s. Thus, regarding the moment of the second stage beginning, the relative difference between the two model predictions is 5.9%, between the measurements and CST model is 10.5%, and 3.9% between the experiment and PB model.

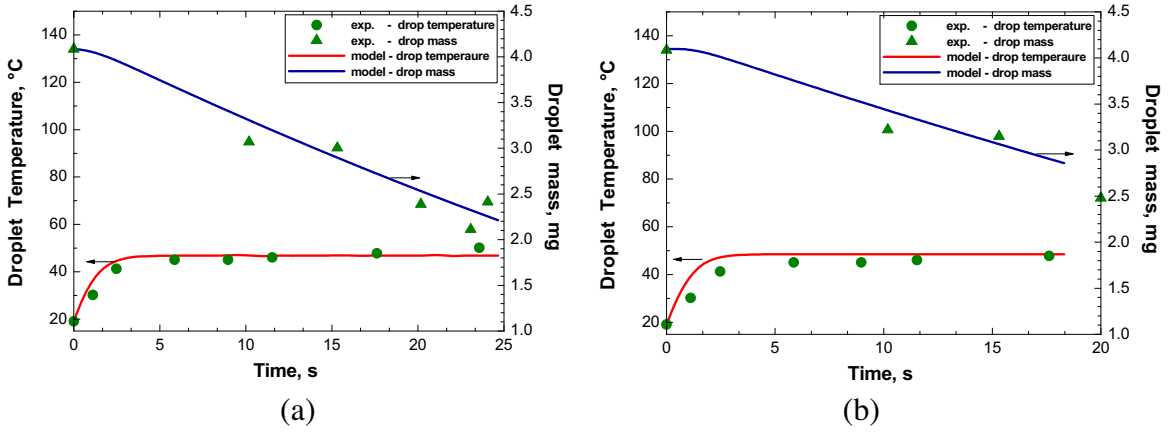

Fig. 8. Temporal evolution of droplet mass and droplet temperature in the first drying stage, T_g = 178 °C. (a) CST model – "locking" of nanoparticles at 18.2 s, first stage duration is 21.5 s; (b) PB model – "locking" of nanoparticles and first stage end are at 18.7 s.

Increase in the air temperature up to 22 °C leads to reduction of both the first drying stage duration and the discrepancies between the two models and the measured values, see Fig. 9b. Particularly, the CST model calculates the duration of the first drying stage equal to 1284 s against 1260 s of PB model and 1170 s of measured value. Consequently, the relative difference between the two model predictions is 1.9%, between the measurements and CST model is 9.7%, and 7.7% between the experiment and PB model.

Additional elevation of the drying temperature up to 35 °C confirms the trends observed before (Fig. 9c). This time the duration of the first drying stage predicted by CST model is equal to 727.5 s, whereas the PB model value is 728 s, and the corresponding experimental point is at 690 s. Thus, the divergence between the two model predictions is as low as 0.07%, between the measurements and CST model is 5.4%, and 5.5% between the experiment and PB model.

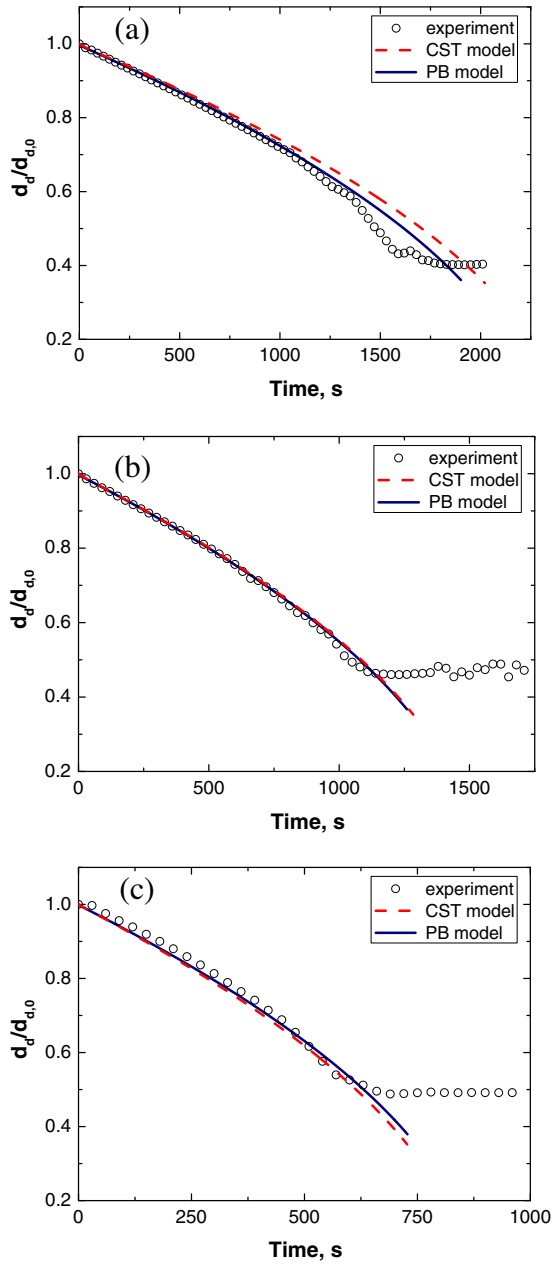

Fig. 9. Comparison between the experimental and calculated evolution of droplet diameter for (a) T_g = 15 °C, (b) T_g = 22 °C and (c) T_g = 35 °C.

6.3. Parametric study and comparison between the two modelling approaches

The setup of single droplet drying that has been used for the validation (see Table 2) is also utilized to compare and verify predictions of different droplet parameters by CST and PB models.

The simulated evolution of silica droplet radius is given in Fig. 10. One can observe that according to CST model, "locking" between the nanoparticles and beginning of transition period occurs at t = 18.2 s, and after that the droplet shrinkage continues whereas the shell thickens until the moment t = 21.5 s when the second drying stage commences. At this point, the strength of the submerged shell becomes sufficient to resist the compressive capillary stress at the shell outer surface. Note that in the present numerical simulations the shell compressive strength has been assumed 100 MPa and this value has influence only on the duration of the transition period but not on the moment of initial "locking" between the suspended particles [19]. For the current conditions, the transition period of shell shrinkage is about 3.3 s or 15.3% of the overall duration of the constant-rate drying period, as predicted by CST simulations. At the same time, the PB model calculates the "locking" between nanoparticles and immediate beginning of the second drying stage at 18.7 s. Therefore, PB model predicts shorter duration of the first drying stage by 13% compared to CST formulation because PB model disregards the possibility of shell shrinkage after the initial "locking" between the suspended particles.

Fig. 11 demonstrates the simulated profiles of solid volume fraction in silica nanosuspension droplet. It can be found that both CST and PB profiles of solid volume fraction are flat at the beginning (t = 0–10 s), owing to the fast intra-droplet liquid motion observed experimentally [14] and considered in the model by assuming $D_p = D_{ls} = 10^{-6}$ m^2 s^{-1}. Later, when the solid *mass* fraction increases up to 0.4, in accordance with [14] the internal circulation ceases due to the formation of viscous gel structure, and this results in significant decrease of diffusion coefficient, see Eq. (40). In turn, this leads to a steep local rise of solid concentration in the vicinity of the droplet surface, since the increase of particles quantity at the surface caused by the droplet drying cannot be equalised now by the slow diffusion of nanoparticles toward the droplet centre. Comparing the profiles calculated by two models given in Fig. 11a and b, one can establish inessential differences between the respective distributions of solid volume fraction as well as close values of locking point calculated by CST and PB models.

Fig. 12 illustrates the history of solid volume fraction at the surface and in the centre of the silica nanosuspension droplet. It can

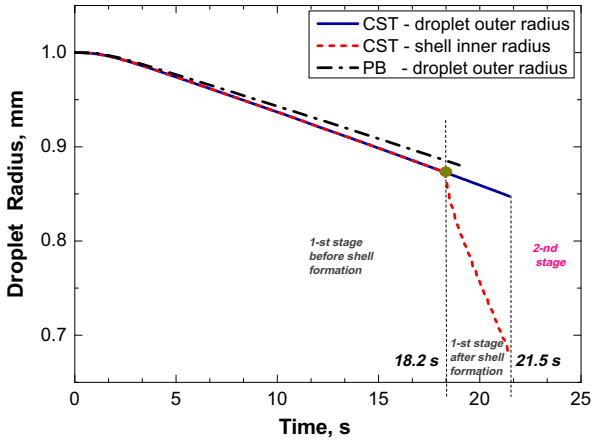

Fig. 10. Simulated evolution of silica droplet radius in first drying stage, T_g = 178 °C.

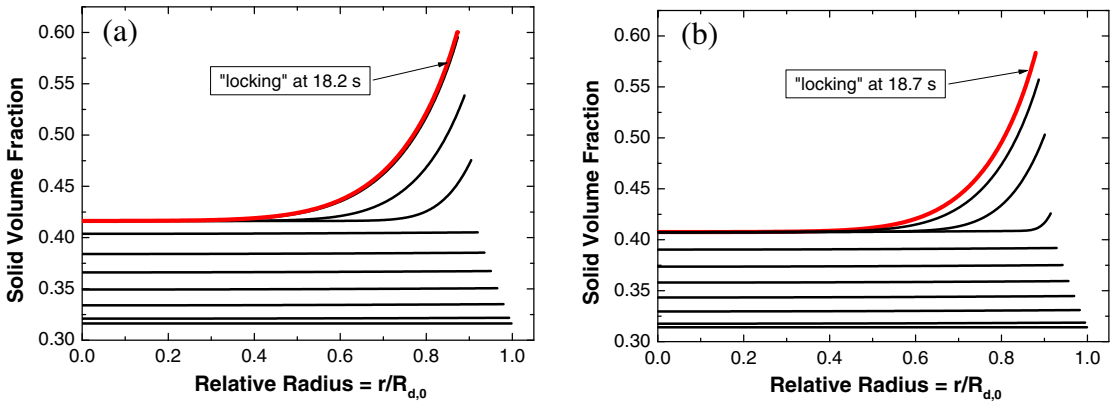

Fig. 11. Time-dependent profiles of solid volume fraction within silica droplet (until shell formation), T_g = 178 °C, data are plotted every 2 s. (a) CST model and (b) PB model.

be found that the temporal evolution of solid volume fraction at the droplet surface predicted by CST model can be divided in three steps. In the first step the volume fraction rises gradually, but after the gel formation at 40% of solid mass fraction (the corresponding solid volume fraction is $\varphi_s = 0.42$, the curve slope increases drastically and, finally, the solid volume fraction remains constant during the shell shrinkage when the maximum concentration of 0.6 is reached. In contrast, the solid volume fraction in the droplet centre stays almost unchanged after the gel formation as solid mass fraction attained 40%. This can be attributed to slow diffusion of particles toward the droplet centre whereas there is a rapid droplet shrinkage leading to the fast increase of solid fraction at the droplet surface. Compared to the CST, the PB model results demonstrate only two steps of gradual and then drastic rise of solid fraction on the droplet surface and corresponding gradual and then steady behaviour of solid volume fraction in the droplet centre. This difference between the CST and PB predictions is explained by the lack of shell shrinkage period in the latter model. In general, the curves predicted by the two models until the locking point are close to each other. Small differences can be explained by different mathematical formulations and numerical implementations of the CST and PB models.

Figs. 13–15 show the results of numerical simulations using the CST and PB models for different temperatures of drying air: 100, 50 and 25 °C. The other setup parameters are as given in Table 2. These calculations demonstrate trends similar to previously observed and discussed for T_g = 178 °C (Figs. 8, 10 and 12). In particular, the PB model predicts shorter duration of the first drying stage compared to the CST formulation, because the PB model does not account for the transition (shell shrinkage) period. Correspondingly, at the end of the first drying stage droplet mass and diameter are bigger for the PB approach. Also, the profiles of solid volume fraction are different at the end of the first drying stage: the CST model predicts shell formation and thickening at the droplet surface, so the surface solid volume fraction evaluated by the CST remains saturated and unchanged in the transition period; at the same time, the values of the solid volume fraction in the droplet centre grow above those calculated by the PB approach. Another interesting aspect is dependence of the shell shrinkage period on the temperature of drying air. Figs. 10, 13 and 14 exhibit decrease of the transition period duration with increase of the drying agent temperature (transition period of 9.7 s for T_g = 50 °C, 7.7 s for T_g = 100 °C and 3.3 s for T_g = 100 °C), but the data in Fig. 15 do not follow this tendency (transition period of 6.5 s for T_g = 25 °C). The explanation of this illusory contradiction is in dependence of the duration of transition period on the rate of shell thickening, and this rate is the function of both the droplet shrinkage rate, $\frac{dR_d}{dt}$, and the value of liquid volume fraction adjacent to the shell interior, $\varphi_l|_{R_{sh}}$, see Eq. (28). The latter parameter expresses the amount of primary particles which may potentially adhere to the shell in the next shell shrinkage act, and thus it may thicken the shell. The magnitude of the $\frac{dR_d}{dt}$ increases with drying temperature, and this is clearly observed if one compares the curve slopes in Figs. 10, 13b, 14b and 15b. On the other hand, the solid volume fraction near the shell interior decreases with drying temperature, as may be concluded from analysis of Figs. 12, 13c, 14c and 15c (bearing in mind that in the transition period the solid volume fraction always grows from the droplet centre towards the shell interior, as it was established by Mezhericher et al. [19]; cf. Fig. 11). Correspondingly, in the vicinity of the shell interior the liquid volume fraction increases with drying temperature. Therefore, when the drying temperature is raised, according to Eq. (28), the numerator with droplet shrinkage rate tends to increase whereas the denominator including liquid volume fraction tends to decrease the magnitude of the shell receding rate, and the combination of these two factors results in the observed mixed behaviour of the transition period duration (Figs. 10, 13–15).

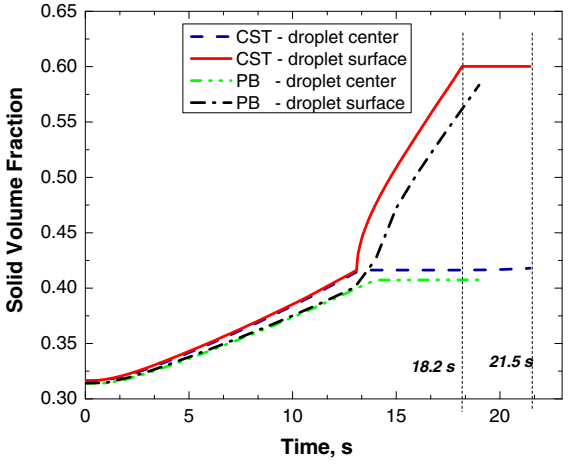

Fig. 12. Simulated evolution of solid volume fraction at surface and in centre of silica droplet in the 1-st drying stage, T_g = 178 °C.

6.4. Implementation of nanoparticle aggregation in PB model

As previously shown, both the CST and the PB models gave a good agreement with experimental data from Nešić and Vodnik [15]. In this comparison, the diffusion coefficient from Nešić and Vodnik [15], which is an empirical one, was used (Eq. (40)).

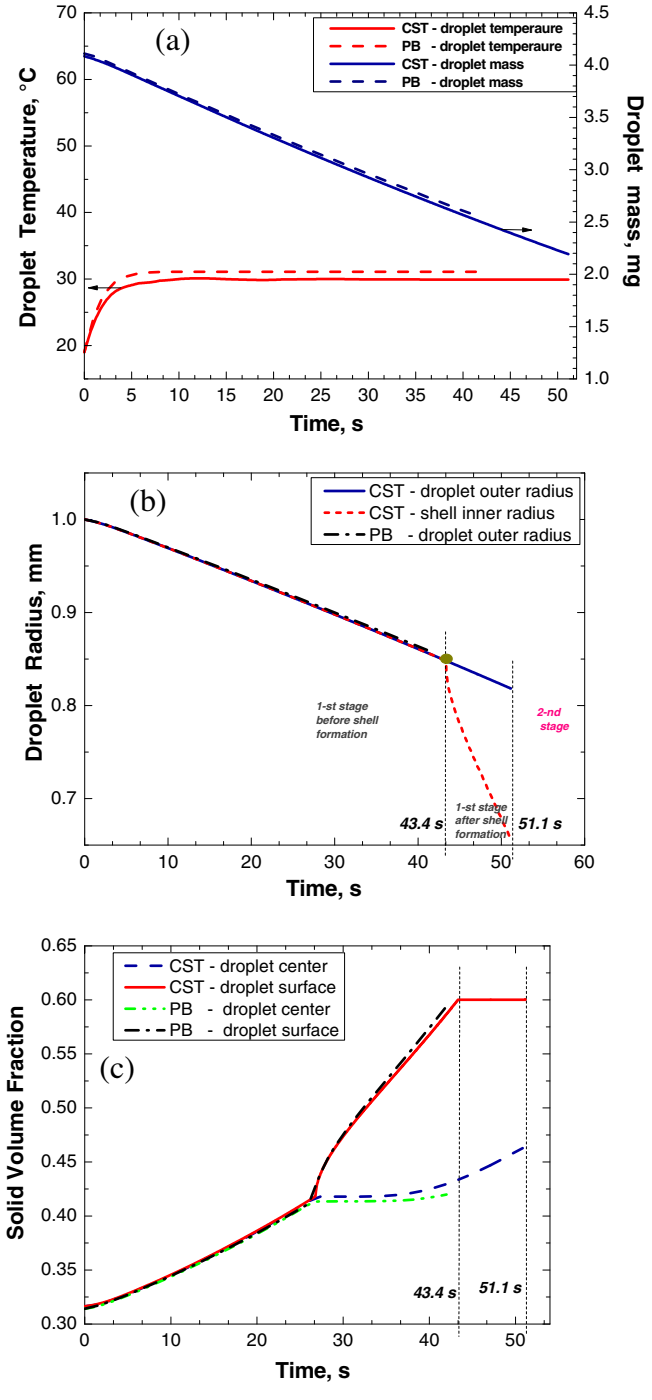

Fig. 13. Calculated history of silica droplet drying at T_g = 100 °C in the first drying stage. (a) Evolution of the droplet mass and droplet temperature; CST model – "locking" of nanoparticles at 43.4 s, first stage duration is 51.1 s, PB model – both "locking" of nanoparticles and first stage end are at 42.2 s. (b) Evolution of the droplet radius. (c) Evolution of the solid volume fraction at surface and in centre of the droplet.

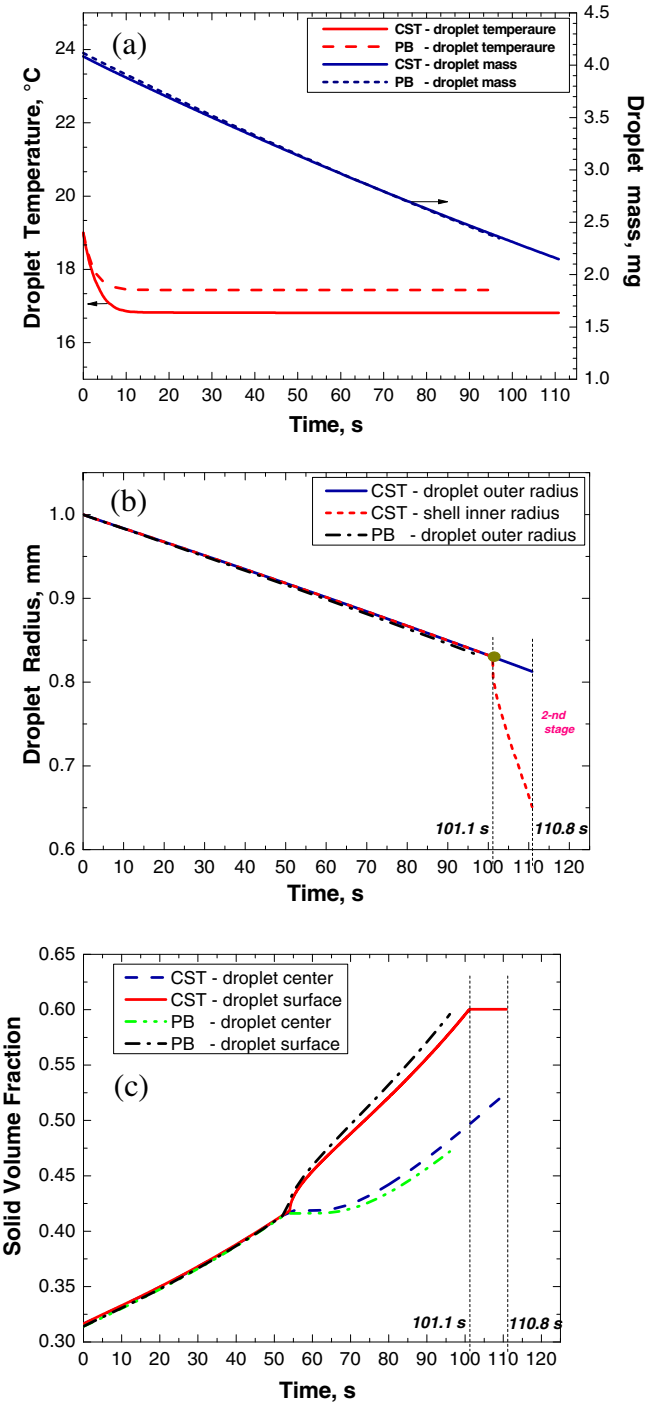

Fig. 14. Calculated history of silica droplet drying at T_g = 50 °C in the first drying stage. (a) Evolution of the droplet mass and droplet temperature; CST model – "locking" of nanoparticles at 101.1 s, first stage duration is 110.8 s. PB model – both "locking" of nanoparticles and first stage end are at 96.3 s. (b) Evolution of the droplet radius. (c) Evolution of the solid volume fraction at surface and in centre of the droplet.

One advantage of the PB model is the ability to study the influence of aggregation on the drying process. To investigate this influence, a size dependent diffusion coefficient has to be used. In the case of nanoparticles the Stokes–Einstein equation can be applied [51]:

$$D_p = \frac{k_B T_d}{3\pi\mu_l d_{pp}}. \quad (41)$$

In the following we investigate whether the Stokes–Einstein equation can also be used to describe the experimental data from Nešić, or not. Fig. 16 demonstrates a comparison between the empirical diffusion coefficient from Nešić according to Eq. (40) and the Stokes–Einstein diffusion coefficient (Eq. (41)) for 16 nm particles; note that the Stokes–Einstein diffusion coefficient does not depend on liquid mass fraction. As one can find, the Stokes

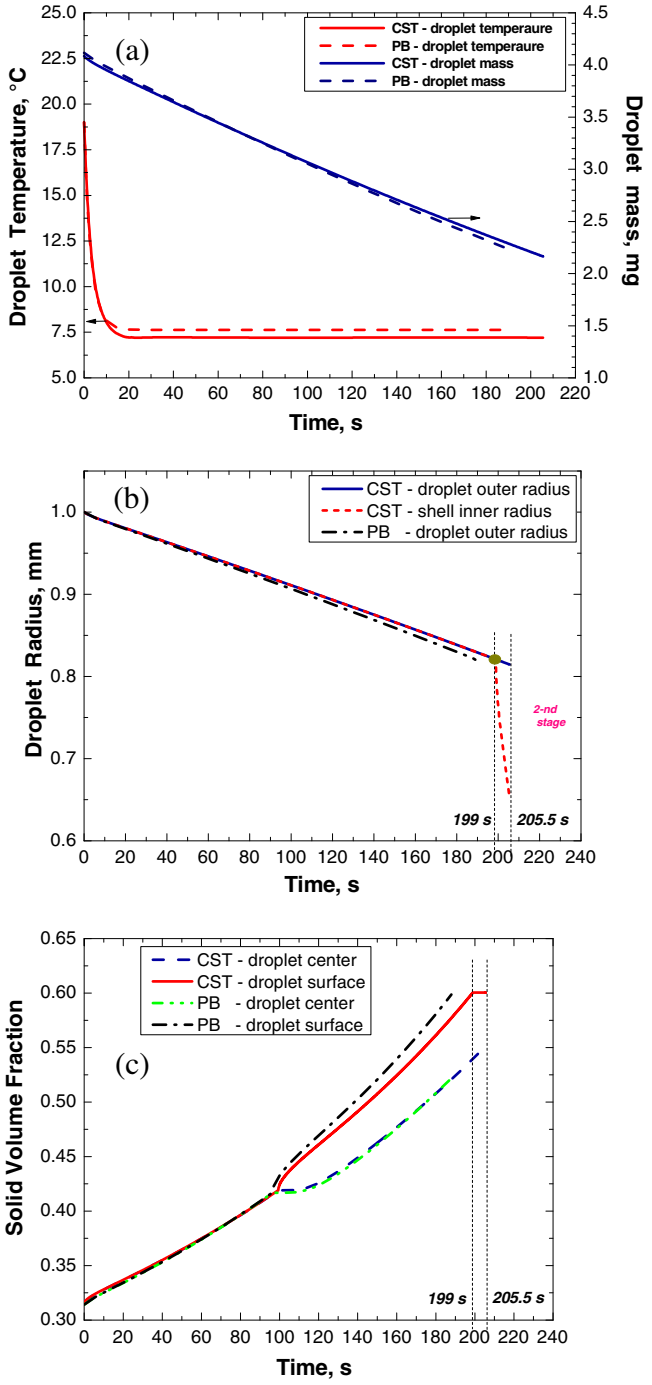

Fig. 15. Calculated history of silica droplet drying at $T_g = 25$ °C in the first drying stage. (a) Evolution of the droplet mass and droplet temperature; CST model – "locking" of nanoparticles at 199 s, first stage duration is 205.5 s. PB model – both "locking" of nanoparticles and first stage end are at 188.5 s. (b) Evolution of the droplet radius. (c) Evolution of the solid volume fraction at surface and in centre of the droplet.

Einstein diffusion coefficient for 16 nm particles is much smaller than the diffusion coefficient from Nešić, even at lower liquid mass fractions.

It is obvious that using the Stokes–Einstein diffusion coefficient from the beginning on results in much earlier locking points (about 1.9 s without aggregation). Even the usage of Stokes–Einstein from the point of gel formation, when the liquid mass fraction is equal to 0.6, would lead to earlier locking points than these given in Figs. 8, 11, 13–15.

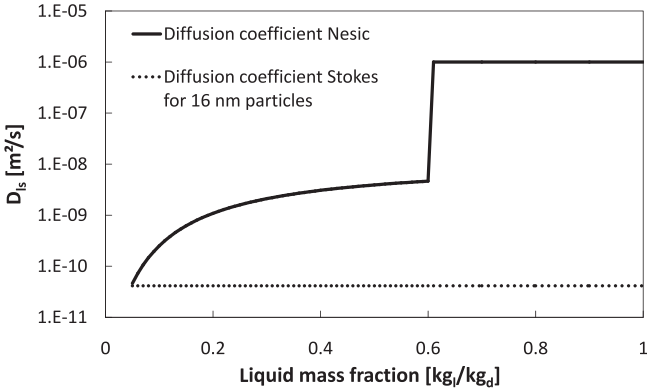

Fig. 16. Comparison between the Nešić and the Stokes–Einstein diffusion coefficients (for 16 nm particles).

To avoid these discrepancies we multiply the Stokes–Einstein diffusion coefficient with a factor given by

$$A = \frac{D_{p,Nesic}(\omega_l = 0.6)}{D_{p,Stokes}}, \tag{42}$$

and apply the following diffusion coefficient:

$$D_p = \begin{cases} 10^{-6}, & \omega_l > 0.6; \\ A\frac{k_B T_d}{3\pi\mu_l d_{pp}}, & \omega_l \leqslant 0.6. \end{cases} \tag{43}$$

Without aggregation, the locking point is now occurring later on than when using the Nešić diffusion coefficient (see in Fig. 17), as the diffusion coefficient according to Eq. (43) remains constant after the point of gel formation. However, the empirically observed decrease of the Nešić diffusion coefficient after gel formation can also be simulated by switching on aggregation.

Respective simulations were conducted with four different values of a constant aggregation kernel. The results in Fig. 17 show that the locking time gets shorter with increasing aggregation efficiency, due to the more restricted mobility of the larger particles inside the droplet.

The locking point $t_{lock} = 18.5$ s with the aggregation kernel of $\beta^* = \beta_0 = 0.05$ 1/s is the closest to the locking time resulting from the Nešić diffusion coefficient. For this aggregation efficiency, more detailed simulation results are shown in Figs. 18–21. It is obvious that external heat and mass transfer during the first drying stage are not influenced by the diffusion coefficient in the droplet. Thus, droplet mass and droplet temperature (Fig. 18) are showing the

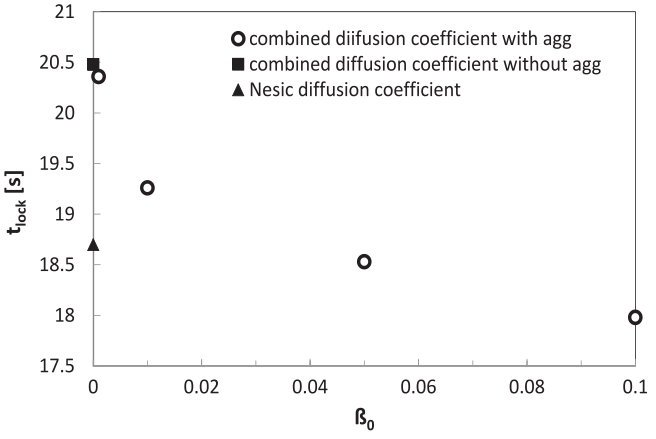

Fig. 17. Comparison of locking points calculated with different values of the constant aggregation kernel (PB model, the setup data are given in Table 2).

same results as in Fig. 8b. The same applies for the droplet radius in Fig. 19.

The simulated time-dependent profiles of solid volume fraction in silica droplet are demonstrated in Fig. 20. Similarly to Fig. 11b, it can be found that the concentration profiles are flat at the beginning owing to the fast intra-droplet liquid motion taken into account by the very large diffusion coefficient ($D_p = 10^{-6}$ m^2/s) before gel formation. As soon as the solid mass fraction has increased to 0.4, the point of gel formation, the diffusion coefficient decreases substantially, see Eq. (43). In turn, this leads to a steep local rise of solids concentration near the droplet surface, since the increase of particle number at the surface caused by the droplet drying cannot any more be equalised by the slow diffusion of nanoparticles toward the droplet centre.

The change of solids volume fraction in the centre and on the surface of the silica droplet is shown in Fig. 21. Similarly to Fig. 12 (PB approach with the Nešić diffusion coefficient), the temporal evolution of solids volume fraction on the droplet surface can be divided in two periods. In the first period the volume fraction increases only slightly. There is no significant difference in solids volume fraction between droplet centre and the droplet surface, due to the high diffusion coefficient. After the gel formation at 40% of solids mass fraction (corresponding to about 42% of solid volume fraction), the curve slope for the droplet surface increases radically. In contrast, the solids volume fraction in the droplet centre stays almost unchanged after gel formation. This can be explained by slow diffusion of particles toward the droplet centre, whereas on the surface there is a rapid shrinkage process leading to the fast increase of solid fraction.

Compared to the simulations with the original diffusion coefficient from Nešić, the curves computed by the PB model with an aggregation kernel of $\beta^* = \beta_0 = 0.05$ 1/s look very similar, and the resulting locking points are very close to each other. This shows that the PB model can describe the experimental data of Nešić and Vodnik [15] not only when using their empirical diffusion coefficients without aggregation, but also when implementing aggregation to physically explain the decrease of particle mobility with increasing solids content after the gelation point.

A step-by-step analysis of how the concentration profiles and the locking points change by the separate or combined action of droplet drying, diffusion and aggregation of suspended primary particles has recently been presented by Bück et al. [25]. The influ-

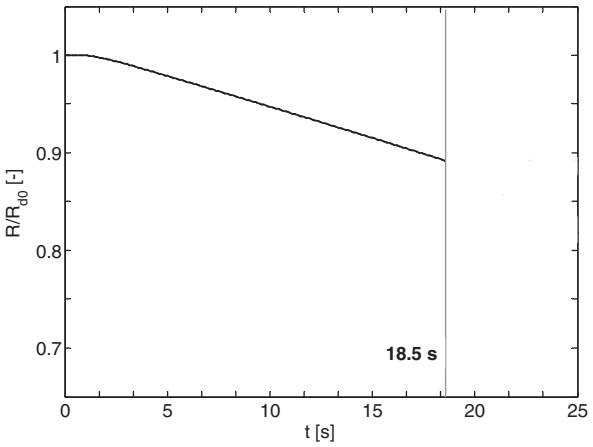

Fig. 19. Temporal evolution of silica droplet radius in the first drying stage according to the PB model with aggregation ($\beta^* = \beta_0 = 0.05$ 1/s). Simulation parameters are the same as for Fig. 18.

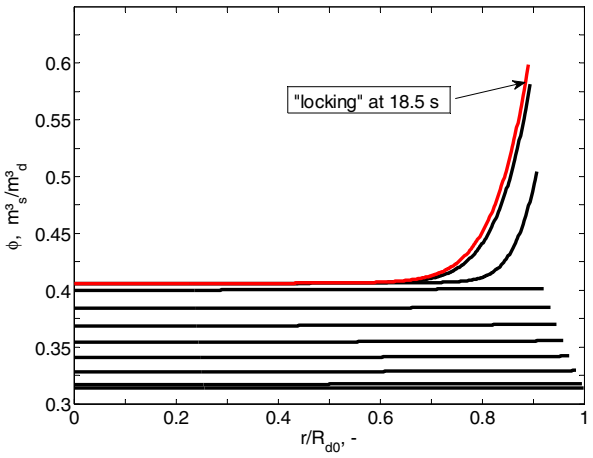

Fig. 20. Time-dependent profiles of solid volume fraction within silica droplet until shell formation according to the PB model with aggregation ($\beta^* = \beta_0 = 0.05$ 1/s). Simulation parameters are the same as for Fig. 18.

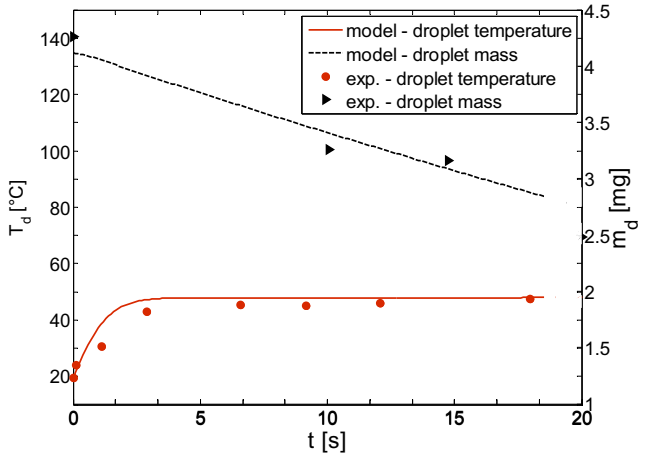

Fig. 18. Temporal evolution of droplet mass and droplet temperature in the first drying stage. Comparison of predictions of the PB model with aggregation ($\beta^* = \beta_0 = 0.05$ 1/s) and diffusion coefficients according to Eq. (43) with experimental data from Nešić and Vodnik [15], see Table 2. The locking point is predicted at 18.5 s.

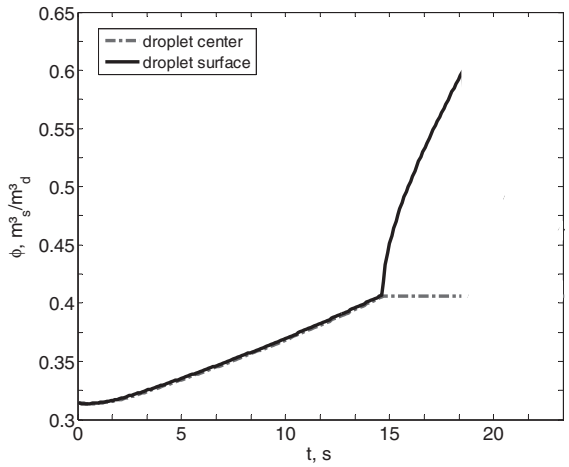

Fig. 21. Temporal evolution of solids volume fraction at the surface and in the centre of silica droplet according to the PB model with aggregation ($\beta^* = \beta_0 = 0.05$ 1/s). Simulation parameters are the same as for Fig. 18.

ence of aggregation kinetics on porosity profiles in the resulting dry particles has also been discussed in the same paper.

7. Conclusion

The present contribution reports on comparison and verification of two different approaches of intra-droplet mass transfer description for nanosuspension droplet drying in constant-rate period. The first approach is continuous species transport (CST) modelling which is based on continuous description of coupled external heat and mass transfer from gas to droplet and species transport equation for intra-droplet mass transfer of nanoparticles. The second approach is population balance (PB) model underpinned by continuous description of coupled external heat and mass transfer from gas to droplet and population balance approach for the intra-droplet mass transfer phenomenon.

The CST model considers two morphological periods of the first drying stage: before shell formation and after the shell formation; the latter is known as transition period involving shell shrinkage [19]. Further, the moment of initial "locking" between nanoparticles into a shell at droplet surface is connected with the saturated value of solid volume fraction. The intra-droplet mass transfer of nanoparticles is described by continuous species transport equation which has been simplified to the form of one-dimensional Fick's diffusion law.

In an alternative approach, population balances were used to describe drying and internal diffusion that take place simultaneously with nanoparticle aggregation within the droplet. This PB approach is novel, because previous literature on population dynamics refers only to growth in drying droplets, not to aggregation. If aggregation is switched off, PB approach becomes essentially identical to the previously discussed CST model during the first stage of drying, so that it can also describe published experimental data using the same empirical diffusion coefficients. Such empirical diffusion coefficients are known to decrease with increasing solids mass fraction after the so-called gelation point. This dependency can be captured by the population balance approach without any need of empirical fitting apart from the selection of some appropriate efficiency in a constant aggregation kernel. The reason is that diffusion and aggregation are interrelated in the population balance approach, with a higher mobility for small and a lower mobility for large aggregates. Consequently, the decrease of diffusion coefficient after the gelation point is attributed to the increasing size of aggregates and calculated on first principles, instead of being correlated with the increasing solid mass fraction.

It is noted, however, that in contrast to CST formulation, the PB model predicts a shorter first drying stage because it does not consider the transition period of shell shrinkage and determines the duration of the first drying stage by simply using the moment of initial locking between the nanoparticles on the droplet surface. On the other hand, as opposed to CST model neglecting the aggregation effects between suspended particles, the developed population balance approach enables to separate the effects of droplet drying (moving boundary), diffusion and aggregation of nanoparticles, so that they can be individually studied and assessed. Morphological features of the emerging particle become accessible, such as the radial profiles of primary particle aggregate size and porosity (cf. [25]).

Assuming that nanoparticles are initially evenly distributed within a single droplet and do not aggregate during the drying process, both CST and PB models have been successively validated using published experimental data of Nešić and Vodnik [15] for 2 mm aqueous silica droplet. This droplet consisted of 16 nm monosized SiO_2 spheres, which were homogeneously suspended in water and produced 30% initial solid content.

Comparing the temporal evolution of solid concentration profiles predicted by the two models for the literature data, inessential differences among the respective distributions of solid volume fraction as well as close values of locking point have been observed. Furthermore, the analysis of calculated time-change of solid volume fraction in the centre and on the surface of the silica droplet has shown similar trends predicted by the CST and PB models until the locking point, and small distinctions are explained by different mathematical formulations and numerical implementations of the two modelling approaches. The only contrast between the CST and PB models is the predicted duration of the first drying stage, which has been found to be about 23% longer in the case of CST approach. Such divergence is explained by the absence of shell shrinkage period in the current PB formulation.

Acknowledgement

The authors appreciatively acknowledge the financial support of the present work from GIF – German-Israeli Foundation for Scientific Research and Development under Grant No. 952 –19.10/2007.

References

[1] A.S. Mujumdar (Ed.), Handbook of Industrial Drying, third ed., CRC Press, 2006.
[2] V.V. Patil, P.P. Dandekar, V.B. Patravale, B.N. Thorat, Freeze drying: potential for powdered nanoparticulate product, Dry. Technol.: Int. J. 28 (5) (2010) 624–635.
[3] Y. He, Y. Huang, W. Wang, Y. Cheng, Integrating micromixer precipitation and electrospray drying toward continuous production of drug nanoparticles, Chem. Eng. J. 168 (2) (2011) 931–937.
[4] N. Ellis, C.U. Yurteri, J.R. van Ommen, Continuous process to deposit nanoparticles onto microparticles, Chem. Eng. J. 181–182 (1) (2012) 798–805.
[5] L.-Y. Lin, H. Bai, Aerosol processing of low-cost mesoporous silica spherical particles from photonic industrial waste powder for CO_2 capture, Chem. Eng. J. 197 (15) (2012) 215–222.
[6] W.E. Ranz, W.R. Marshall Jr., Evaporation from drops, Chem. Eng. Prog. 48 (1952) 141–180.
[7] W.R. Marshall Jr., Heat and mass transfer in spray drying, Trans. ASME 77 (1955) 1377–1385.
[8] A.M. Trommelen, E.J. Crosby, Evaporation and drying of drops in superheated vapours, AIChE J. 16 (5) (1970) 857–867.
[9] N. Abuaf, F.W. Staub, Drying of liquid–solid slurry droplets, in: Drying'86, vol. 1, Washington, 1986, pp. 277–284.
[10] B. Abramzon, W.A. Sirignano, Droplet vaporization model for spray combustion calculations, Int. J. Heat Mass Transf. 32 (1989) 1605–1618.
[11] D.E. Walton, The evaporation of water droplets: a single droplet drying experiment, Dry. Technol. 22 (2004) 431–456.
[12] M. Mezhericher, A. Levy, I. Borde, The influence of thermal radiation on drying of single droplet/wet particle, Dry. Technol. 26 (1) (2008) 78–89.
[13] Y. Sano, R.B. Keey, The drying of a spherical particle containing colloidal material into a hollow sphere, Chem. Eng. Sci. 37 (6) (1982) 881–889.
[14] S. Nešić, The evaporation of single droplets – experiments and modelling, in: A.S. Mujumdar (Ed.), Drying '89, Hemisphere, New York, 1990, pp. 386–393.
[15] S. Nešić, J. Vodnik, Kinetics of droplet evaporation, Chem. Eng. Sci. 46 (1991) 527–537.
[16] T. Furuta, H. Hayashi, T. Ohashi, Some criteria of spray dryer design for food liquid, Dry. Technol. 12 (1–2) (1994) 151–177.
[17] H. Liang, K. Shinohara, H. Minoshima, K. Matsushima, Analysis of constant rate period of spray drying of slurry, Chem. Eng. Sci. 56 (2001) 2205–2213.
[18] K. Jorgensen, A.D. Jensen, J. Sloth, K. Dam-Johansen, P. Bach, Letter to editor: comments to "Analysis of constant rate period of spray drying of slurry" by Liang et al., 2001, Chem. Eng. Sci. 61 (2006) 2096–2100.
[19] M. Mezhericher, A. Levy, I. Borde, Modelling the morphological evolution of nanosuspension droplet in constant-rate drying stage, Chem. Eng. Sci. 66 (5) (2011) 884–896.
[20] P. Seydel, A. Sengespeick, J. Blomer, J. Bertling, Experiment and mathematical modeling of solid formation at spray drying, Chem. Eng. Technol. 27 (5) (2004) 505–510.
[21] P. Seydel, J. Blomer, J. Bertling, Modelling particle formation at spray drying using population balance, Dry. Technol. 24 (2006) 137–146.
[22] C.S. Handscomb, M. Kraft, A.E. Bayly, A new model for the drying of droplets containing suspended solids, Chem. Eng. Sci. 64 (4) (2009) 628–637.
[23] C.S. Handscomb, M. Kraft, A.E. Bayly, A new model for the drying of droplets containing suspended solids after shell formation, Chem. Eng. Sci. 64 (2) (2009) 228–246.
[24] C.S. Handscomb, M. Kraft, Simulating the structural evolution of droplets following shell formation, Chem. Eng. Sci. 65 (2) (2010) 713–725.

[25] A. Bück, M. Peglow, M. Naumann, E. Tsotsas, A population balance model for drying of droplets containing aggregating nanoparticles, AIChE J., in press. http://dx.doi.org/10.1002/aic.13726.
[26] F. Iskandar, I.W. Lenggoro, B. Xia, K. Okuyama, Functional nanostructured silica powders derived from colloidal suspensions by sol spraying, J. Nanopart. Res. 3 (2001) 263–270.
[27] W.N. Wang, I.W. Lenggoro, K. Okuyama, Dispersion and aggregation of nanoparticles derived from colloidal droplets under low-pressure conditions, J. Colloid Interface Sci. 288 (2005) 423–431.
[28] P. Perré, Multiscale aspects of heat and mass transfer during drying, Transp. Porous Media 66 (1–2) (2007) 59–76.
[29] M. Mezhericher, A. Levy, I. Borde, Theoretical drying model of single droplets containing insoluble or dissolved solids, Dry. Technol. 25 (6) (2007) 1025–1032.
[30] Y. Cengel, M. Boles, Thermodynamics: An Engineering Approach, McGraw-Hill, 1998.
[31] G.M. Harpole, Droplet evaporation in high temperature environments, J. Heat Transfer 103 (1) (1981) 86–91.
[32] V.A. Grigoriev, V. M Zorin, Thermal Engineering Handbook, vol. 1, second ed., Energoatomizdat, Moscow, 1988 (in Russian).
[33] E.L. Cussler, Diffusion Mass Transfer in Fluid Systems, Cambridge University Press, New York, 2009.
[34] J. Sloth et al., Model based analysis of the drying of a single solution droplet in an ultrasonic levitator, Chem. Eng. Sci. 61 (2006) 2701–2709.
[35] S. Timoshenko, J.N. Goodier, Theory of Elasticity, McGraw-Hill, New York, 1951.
[36] C. Orr Jr., Particulate Technology, Macmillan Company, New York, 1996.
[37] D. Megias-Alguacil, L.J. Gauckler, Capillary and van der Waals forces between uncharged colloidal particles linked by a liquid bridge, Colloid Polym. Sci. 288 (2010) 133–139.
[38] D. Ramkrishna, Population Balances: Theory and Application to Particulate Systems in Engineering, Academic Press, 2000.
[39] R.J. LeVeque, Finite Volume Methods for Hyperbolic Problems, Cambridge University Press, 2004.
[40] A.D. Polyanin, A.V. Manzhirov, Handbook of Mathematics for Engineers and Scientists, Taylor and Francis Group, Chapman and Hall, Boca Raton, 2007.
[41] J.C. Butcher, Numerical Methods for Ordinary Differential Equations, second ed., Wiley, 2008.
[42] E.A. Moyano, A.F. Scarpettini, Numerical stability study and error estimation for two implicit schemes in a moving boundary problem, Numer. Meth. Partial Diff. Eq. 16 (2000) 42–61.
[43] J. Kumar, M. Peglow, G. Warnecke, S. Heinrich, L. Mörl, Improved accuracy and convergence of discretized population balance for aggregation: the cell average technique, Chem. Eng. Sci. 61 (2006) 3327–3342.
[44] J. Crank, Free and Moving Boundary Problems, Clarendon Press, Oxford, 1996.
[45] R.D. Skeel, M. Berzins, A method for the spatial discretization of parabolic equations in one space variable, SIAM J. Sci. Stat. Comput. 11 (1990) 1–32.
[46] L.F. Shampine, M.W. Reichelt, The MATLAB ODE suite, SIAM J. Sci. Comput. 18 (1) (1997) 1–22.
[47] C. Groenewold, C. Möser, H. Groenewold, E. Tsotsas, Determination of single-particle drying kinetics in an acoustic levitator, Chem. Eng. J. 86 (2002) 217–222.
[48] I. Zbicinski, A. Delag, C. Strumillo, J. Adamiec, Advanced experimental analysis of drying kinetics in spray drying, Chem. Eng. J. 86 (2002) 207–216.
[49] C. Möser, Die Desorption von Ammoniak aus Wassertropfen im Ultraschall-Stehwellenfeld, Magdeburg, Germany, Dissertation, 2001.
[50] H. Rumpf, Particle Technology, Chapman and Hall, London, 1990.
[51] A. Einstein, Über die von der molekularkinetischen Theorie der Wärme geforderte Bewegung von in ruhenden Flüssigkeiten suspendierten Teilchen, Ann. Phys. 17 (1905) 549–560.